NUCLEAR ENGINEERING AND TECHNOLOGY
ISSN / eISSN 1738-5733
Publisher KOREAN NUCLEAR SOC, NUTOPIA BLDG,
342-1 JANGDAE-DONG,
DAEJEON, SOUTH KOREA, 305-308
Volume 26-Issue 1-(2026)
DOI:https://doi.org/10.65613/700506

OPEN ACCESS

Dual Optimization Effect of Axial Magnetic Field and Mechanical Vibration on High Entropy Alloy Coating Properties

Jinfu Jiao , Xiaorong Wang * , Xiaoqin Liu , Chaoqin Wang , Yanda Ding , Fulai Dai a School of Mechanical and Electrical Engineering, Lanzhou Jiaotong University, Lanzhou 730070, China.

* E-mail: Robot_cnc@126.com

Abstract

Critical components of high-end equipment endure severe wear and oxidation under extreme high-temperature conditions, creating an urgent demand for high-performance protective coatings. High-entropy alloy (HEA) coatings show great potential yet suffer from coarse grains, compositional segregation, and insufficient service stability. Herein, WTaNbMo-AlSi HEA coatings were fabricated on Inconel 718 substrates via laser cladding integrated with an axial magnetic field and mechanical vibration, and orthogonal experiments were conducted to systematically explore the dual-field effects on the coating′ s microstructure, mechanical properties, and high-temperature oxidation resistance. The dual fields synergistically regulated melt pool flow and nucleation kinetics, achieving remarkable optimizations: grain size was reduced by 49.58%–62.34%, microhardness increased by 6.72%–23.70%, wear rate decreased by 42.68%, oxidation weight gain at 800°C was cut by 38.6%–52.1%, and interfacial bonding strength was enhanced by 45%, significantly i

mproving service stability. This dual-field collaborative strategy effectively overco mes the inherent drawbacks of HEA coatings, offering a novel technical pathway for their application in critical components of aero-engines and gas turbines.

Keywords: laser cladding; axial magnetic field; mechanical vibration; high-entropy alloy coating

1. Introduction

In modern industrial manufacturing, extreme conditions demand better materi al performance. Critical components in aerospace, energy, and power sectors face complex service environments, leading to surface wear and oxidation failure. Dev eloping high - performance surface protective coatings is a key focus in material s science[1].

High - Entropy Alloys (HEAs) are a novel multi - element alloy system. W ith unique effects, they show excellent high - temperature strength, wear and oxi dation resistance, making them promising for surface protection. Laser cladding i s a mainstream method for preparing HEA coatings[2].

However, HEA coatings have limitations. Their complex composition causes une ven element diffusion and segregation during laser cladding, resulting in coarse d endritic structures and high porosity. These "defect sources" reduce coating de nsity and compromise performance. Conventional HEA coatings also have inadeq uate high - temperature oxidation resistance, restricting their engineering applicati ons[3].

To address these issues, researchers use external field modulation techniques. A xial magnetic fields drive melt pool convection to promote element diffusion and reduce defects. Mechanical vibrations disrupt gradients in the melt pool to facili tate nucleation and suppress segregation. Single - field modulation can improve s

ome properties, but it has limitations and can't comprehensively solve the proble ms of HEA coatings[4]-[6].

2 Materials and Methods

2.1 Experimental Materials

2.1.1 Material Selection and Treatment

The research selected Inconel 718 nickel-based superalloy as the laser claddi ng substrate for its excellent high-temperature strength,oxidation resistance,and cor rosion resistance[7][8].It is widely used in aerospace and energy fields for key co mponents.The substrate size is 100 mm×50 mm×5 mm,designed to meet experim ental operation requirements(e.g.,clamping)and simulate actual components,ensuring practical and instructive experimental results[9].

Table 2-1 Properties of Inconel 718 Nickel-based Superalloy

performance index	numeric value
Density/(g/cm³)	8.22
melting point /℃	1260-1320
Tensile strength at room temperature / MPa	≥1240
Room temperature yield strength / MPa	≥860

performance index	numeric value
Tensile strength at high temperature (650℃)/MPa	≥965
High-temperature yield strength (650℃)/MPa	≥724
elongation /%	≥12
hardness /HRC	≥42

In the alloy system, various elements will have synergistic effects, which ca n endow the alloy with extremely excellent comprehensive properties. Specificall y, nickel exists as the main component in alloys, providing excellent matrix stren gth and toughness, enabling the alloy to maintain stable structure and performanc e under external forces. Chromium plays an important role in alloys, as it can e nhance the alloy's oxidation and corrosion resistance, allowing the alloy to maint ain a good state and be less susceptible to damage in the face of oxidizing and corrosive environments. The addition of iron element also has a unique significan ce, as it can regulate the cost and overall performance of alloys, effectively cont rolling production costs while ensuring alloy performance[10]. Niobium and molyb denum, two elements, can effectively improve the high-temperature strength and hardness of alloys by forming carbides, allowing the alloy to maintain high stren gth and hardness in high-temperature environments and be less prone to deformat

ion. Titanium and aluminum form a dense oxide protective film under high temp erature conditions[11], which can further enhance the alloy's oxidation resistance a nd provide better protection in high-temperature oxidation environments[12]-[16].

2.1.2 Preparation and Characterization of Coating Powders

The coating powder is a blend of WTaNbMo(refractory HEA with high melt ing point,strength,and high-temperature stability)and AlSi40(60wt.%Al[17],40wt.%Si; Al for low density and oxidation resistance,Si for hardness/wear resistance)at an 8:2 mass ratio,activating multiple strengthening mechanisms.Preparation involves c rushing,grinding,sieving to 50–100μm,planetary ball milling(200 rpm,4 h,anhydrous ethanol as dispersant),and vacuum drying(80°C,6 h).SEM/EDS show irregular(sph erical/block-like)particles with uniform size,no agglomeration,and composition mat ching design[18]-[21].

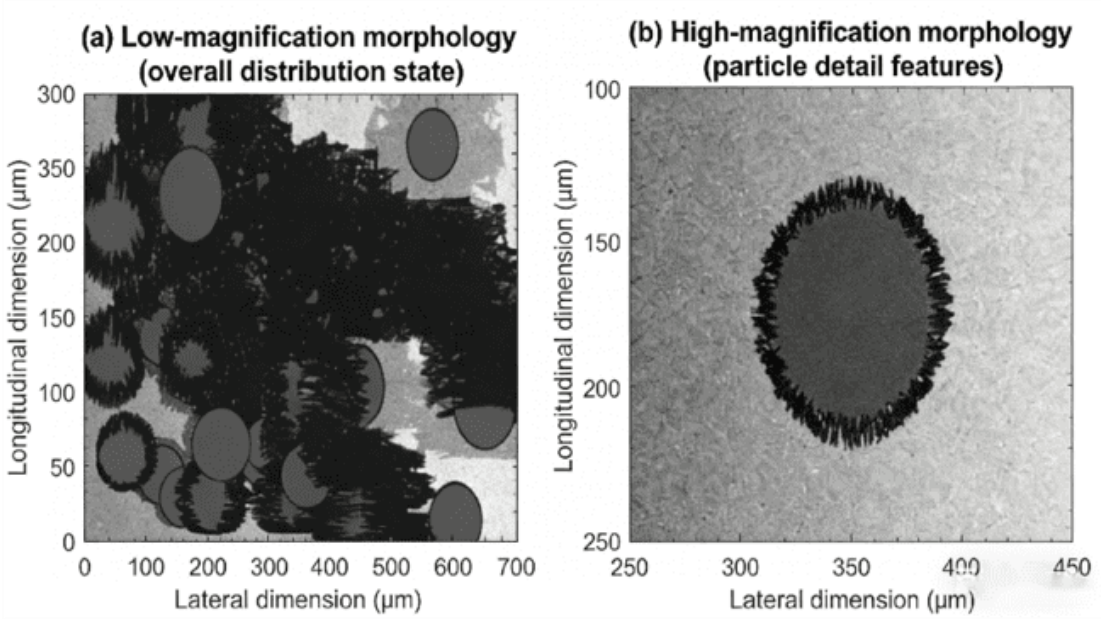

Figure 2-1 SEM morphology of WTaNbMo-AlSi composite powder[22].Note:

(a)Low magnification image showing the overall distribution of the powder;(b)High magnification image revealing the detailed characteristics of the powder particles.

Table 2-2 EDS Analysis Results of EDS Composition for WTaNbMo-AlSi Mixed Powders (wt.%):

element	W	Ta	Nb	Mo	Al	Si	other
design value	20.0	20.0	20.0	20.0	12.0	8.0	0
measured value	19.8	19.9	20.1	20.2	11.8	8.2	0

2.2 Coating Preparation Process

2.2.1 Experimental Equipment

The coating preparation platform comprises IPG-YLR-5000 fiber laser(1070 nm wavelength,5000 W max power[23],4 mm spot),self-designed axial magnetic field device(0/45/90 mT,closed-loop control,water-cooled),mechanical vibration table (0/20/40 kHz,5–15μm amplitude),pneumatic powder feeding system(5–50 g/min,20 g/min in experiment[24]-[28],coaxial nozzle),and PLC control system.The latter synchronously adjusts all parameters and monitors in real time for experiment reliability.[29]-[33].

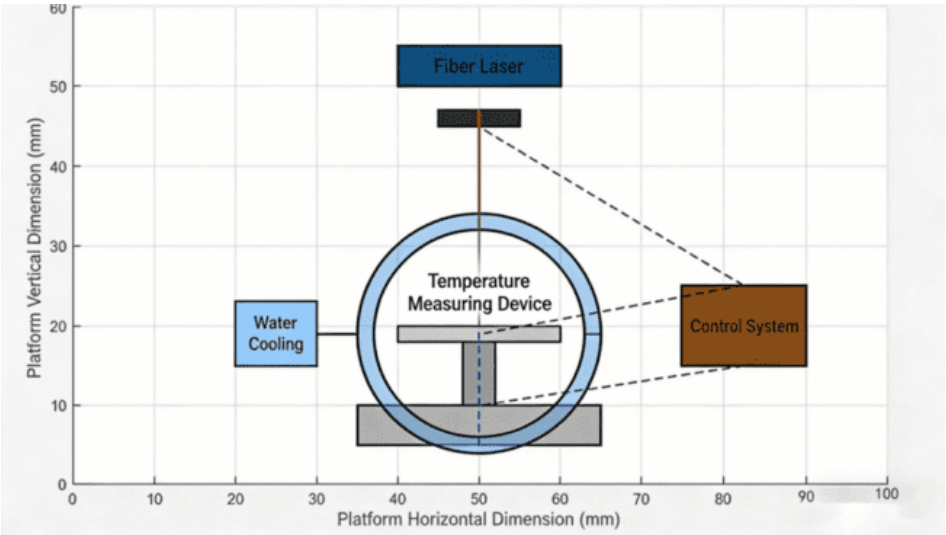

Figure 2-2 Schematic of the Laser Cladding-Axial Magnetic Field-Mechanical Vibration Collaborative Experimental Platform

Note: 1-fiber laser; 2-focusing lens; 3-powder feeding nozzle; 4-axis magnetic field device; 5-mechanical vibration table; 6-substrate; 7-control system; 8-water cooling system.

2.2.2 Process Parameters

(1)Laser Power

When the laser power is too low,the powder cannot be fully melted.This will lead to poor bonding between the coating and the substrate,and a series of problems such as easy peeling of the coating may occur,seriously affecting the quality of laser cladding[34].Conversely,if the laser power is too high,the substrate will over-melt,resulting in an increase in dilution rate.The increase in dilution rate will cause the coating composition to deviate from the original design value,making the coating unable to meet the expected performance requirements.In this experim

ent,to investigate the effect of laser power on the laser cladding effect[35].,the las er power was set to 1.5 kW,2.0 kW,2.5 kW,3.0 kW,and 3.5 kW respectively.Mea nwhile,other parameters were fixed as follows:scanning speed at 5 mm/s,powder f eeding rate at 20 g/min,defocus amount at+2 mm,and no magnetic field or vibrat ion applied during the experiment.After a series of rigorous experiments and deta iled observation and analysis,the results show that when the laser power is in th e range of 2.0~3.0 kW,the coating surface can maintain a flat state,the powder c an be fully melted,and the dilution rate can be controlled within a reasonable ra nge.Based on these experimental results,we determined the suitable range of laser power as 2.0~3.0 kW.In this experiment,considering various factors,we finally se lected 2.5 kW as the fixed power for subsequent related experiments[36].

(2)Scanning Speed

If the scanning speed is too fast,the cooling rate of the molten pool will ac celerate,which will refine the grains.However,an excessively fast scanning speed may also lead to insufficient melting of the powder,thereby affecting the coating quality.On the contrary,when the scanning speed is too slow,the residence time of the molten pool will be prolonged,the grains will become coarse,and the dilutio n rate will increase[37].To study the specific effect of scanning speed on the laser cladding effect,the scanning speed was set to 3 mm/s,4 mm/s,5 mm/s,6 mm/s,an d 7 mm/s respectively in the experiment.Other parameters were kept fixed:laser p

ower at 2.5 kW,powder feeding rate at 20 g/min,defocus amount at+2 mm,and n o magnetic field or vibration applied.The experimental results show that when th e scanning speed is 5 mm/s,the grain size of the coating is in a moderate state,a nd the compactness of the coating is relatively high[38].Therefore,considering vario us factors comprehensively,we determined the scanning speed as 5 mm/s[39].

(3)Defocus Amount

Under positive defocus conditions,the laser spot area increases,and the energy density decreases accordingly.This situation can reduce the over-melting of the s ubstrate to a certain extent,which is conducive to ensuring the quality of the coa ting and the substrate.In contrast,under negative defocus conditions,the energy den sity will concentrate,which is likely to lead to excessive melting depth of the su bstrate and may cause unnecessary damage to the substrate.To find the appropriat e defocus amount,the defocus amount was set to-3 mm,-2 mm,-1 mm,0 mm,+1 mm,+2 mm,and+3 mm respectively in the experiment.Other parameters remained unchanged:laser power at 2.5 kW,scanning speed at 5 mm/s,powder feeding rate at 20 g/min,and no magnetic field or vibration.The experimental results show tha t when the defocus amount is+2 mm,both the depth and width of the molten po ol are in a moderate state,the coating surface quality is good,and no obvious def ects occur.Therefore,we determined the defocus amount as+2 mm[40].

Table 2-3 Orthogonal Test Parameter Combination Table

group	magnetic field intensity /mT	frequency of oscillation /kHz	preheat temperature /℃	cooling-down method
A1	0	0	200	air cooling
A2	0	20	200	air cooling
A3	0	40	200	air cooling
B1	45	0	200	air cooling
B2	45	20	200	air cooling
B3	45	40	200	air cooling
C1	90	0	200	air cooling
C2	90	20	200	air cooling
C3	90	40	200	air cooling

2.3 Characterization Methods and Performance Testing

2.3.1 Macroscopic Morphology and Dimensional Measurement

The surface of the coating and the macroscopic morphology of its cross - section were carefully observed by making use of an optical microscope. The pur

pose of this observation was to thoroughly analyze the surface flatness and the d istribution of defects under various different process parameters. Different process parameters can have a significant impact on the quality of the coating, and by observing these aspects, we can gain a better understanding of how the coating behaves under different conditions.

The melt width and melt depth of the coating were measured with the help of Image - Pro Plus image analysis software. This software is a powerful tool th at can accurately measure the relevant parameters of the coating in the images. I n each sample, five distinct positions were deliberately selected for measurement. Selecting multiple positions helps to reduce the measurement error caused by loc al differences in the coating. After the measurements at these five positions were completed, the average value was calculated and taken as the final result. This averaging method can make the measurement result more representative and relia ble.

The dilution rate is calculated by adopting the area method. This method in volves precisely measuring the ratio of the area of the melted substrate to the to tal cross - sectional area of the coating. The area of the melted substrate and th e total cross - sectional area of the coating are two key factors in calculating th e dilution rate. By accurately measuring these two areas, we can obtain a more accurate dilution rate. The calculation formula for this is as follows:

$$D = \frac{A_b}{A_c + A_b} \times 100\%$$

Where D is the dilution ratio $A_b A_c$(%), A is the area of the substrate melti ng region (mm²), and A is the area of the coating region (mm²).

The porosity was calculated by Image-Pro Plus software to analyze the SE M image of the cross-section of the coating, and the ratio of the porosity area t o the total image area was calculated. Three different cross-sections were selecte d for each sample, and five images were taken for each cross-section, and the a verage value was taken as the porosity of the coating.

2.3.2 Microstructural Characterization

The surface and cross-sectional microstructures of the coating were meticulo usly examined using a ZEISS Sigma 300 scanning electron microscope (SEM) to analyze grain morphology, phase distribution, defect characteristics, and interfaci al bonding between the coating and substrate. The SEM was operated at 20 kV with an 8 mm working distance. Element distribution in the coating was semi-qu antitatively analyzed via energy dispersive spectrometer (EDS), with elemental sc ans performed in both the central and interface regions of the cross-section to re veal element diffusion and segregation patterns.

The EBSD test was performed using the EBSD detector integrated with the SEM. Prior to testing, the sample cross-section underwent electrolytic polishing t o achieve a smooth test surface. The test parameters were: acceleration voltage o

f 20 kV, step size of 0.5 μm, and scanning area of 500 μm × 500 μm. The E BSD data were processed using HKL Channel 5 software to generate grain size distribution maps and polarograms, enabling quantitative analysis of the effects of axial magnetic fields and mechanical vibrations on grain refinement and texture evolution.

The XRD analysis was performed using a Cu target with a tube voltage of 40 kV, tube current of 30 mA, and a scanning range of 2θ = 20° to 80° at a r ate of 5°/min with a step size of 0.02°. The XRD spectra were processed with J ade 6.5 software to identify the phase types, content, and structural variations in the coating, calculate the half-width of the diffraction peaks, and analyze grain r efinement and lattice distortion.

2.3.3 Mechanical Property Testing

The coating hardness was measured using an MH-5L microhardness tester. D uring testing, a 500g load was applied and maintained for 15 seconds to ensure accurate and stable hardness measurements. For each cross-section of the coating sample, ten measurement points were selected at 100μm intervals along the verti cal direction from the substrate to the coating surface. The average value of thes e points was taken as the hardness measurement for the sample to minimize erro rs and ensure data reliability.

The wear test employed a ball-disc friction method with GCr15 steel balls a

s the friction pair. Test parameters were set as follows: load of 20 N, rotational speed of 200 r/min, grinding length of 500 μm, experimental temperature at roo m temperature, and no lubrication condition. The sample mass was measured bef ore and after the experiment using an electronic balance, and the mass loss was calculated to determine the wear rate. The wear rate calculation formula is as fol lows:

$$W = \frac{\Delta m}{\rho \times L}$$

In this study, W denotes the wear $\Delta m\rho$rate (mg/m), m represents mass loss (mg), ρ indicates coating density (g/cm³), and L stands for grinding length (m). After the experiment, the wear surface morphology was observed via SEM to an alyze the wear mechanism.

2.3.4 High Temperature Oxidation Performance Test

In a box-type resistance furnace, high-temperature oxidation tests were condu cted on coated samples cut into 10 mm × 10 mm × 5 mm dimensions. Prior t o testing, the sample surfaces were ground and polished to remove oxide scales, followed by 10-minute ultrasonic cleaning with acetone. After drying, the initial mass was measured. The samples were then placed in a corundum crucible and subjected to oxidation at 800°C for 28 hours. During the experiment, samples w ere removed every 4 hours, cooled to room temperature, and weighed to precisel y calculate the weight gain (mg/cm²). Oxidation kinetics curves were subsequentl

y plotted.

After the oxidation experiment, the surface and cross-sectional morphology o f the oxide film were observed using SEM, the composition of the oxide film w as analyzed by EDS, and the phase composition of the oxide film was identified by XRD. The thickness of the oxide film was measured using Image-Pro Plus software, with five different positions selected for each sample, and the average value was taken as the oxide film thickness.

3. Results and Discussion

3.1 Macrostructure and Microstructure of the Coating

3.1.1 Macro Imaging Quality

The macroscopic morphology and related parameters of the high entropy all oy coatings prepared under different process parameters are observed. The results show that the external field has a significant effect on the coating quality.

In the absence of magnetic field vibration (Group A1), the coating surface e xhibited pronounced pits and pores (Figure 3-1a), attributable to gas escape ineffi ciency in the molten pool and uneven solidification during laser cladding. Calcul ations revealed a dilution rate of 18.7% for this group, indicating excessive incor poration of substrate components into the coating, which compromised its origina l design composition and performance. The coating surface displayed significant r oughness with a measured Ra value of 3.2μm, along with localized unmelted po

wder particles, resulting in suboptimal overall formation quality.

Under the 45 mT magnetic field and 20 kHz vibration (Group B2), the coat ing exhibited a smooth and dense surface with no visible pits or pores. The por osity was reduced to 3.2%, and the dilution rate decreased to 12.3% (Figure 3-1 b). The surface roughness (Ra) was minimized to 1.5 μm, indicating significant i mprovement in formation quality. The combined effect of the Lorentz force gener ated by the magnetic field and the acoustic flow effect induced by vibration faci litated gas expulsion from the molten pool, enhanced its fluidity, and promoted more uniform solidification. This effectively reduced both porosity and dilution ra tes.

When the magnetic field strength was increased to 90 mT with a vibration frequency of 40 kHz (Group C3), the surface quality of the coating was further improved, with a porosity of only 2.1% and a dilution rate reduced to 10.5%. T he coating surface was smooth and flat, with no obvious defects, and a Ra valu e of 1.2 μm, demonstrating excellent macroscopic forming quality.

Table 3-1 Comparison of Macroforming Quality Parameters of High Entropy Allo y Coatings

group	melting width /mm	depth of fusion /mm	dilution /%	porosity /%	Surface roughness Ra/μm
A1	3.25	0.85	18.7	8.9	3.2
B2	3.52	0.72	12.3	3.2	1.5
C3	3.68	0.65	10.5	2.1	1.2

The high-frequency disturbances induced by vibration enhance the complexity and uniformity of convection within the molten pool, reducing variations in the width of the molten layer and improving the quality uniformity of the coating. By calculating the standard deviation of the coating width at different vibration frequencies, the standard deviation for Group A1 was 0.21 mm, while for Group A3 it decreased to 0.18 mm, demonstrating a significant improvement in uniformity.

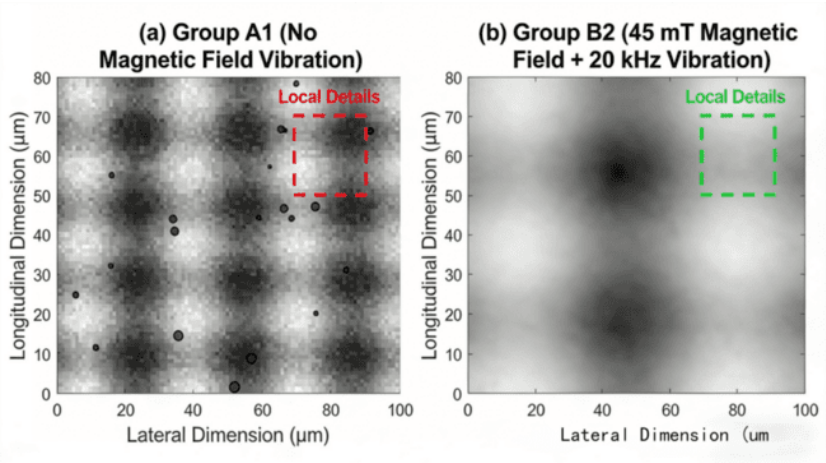

Figure 3-1 (a) Macroscopic surface morphology of Group A1 (vibration without magnetic field) and (b) Group B2 coating

3.1.2 Microstructural Characteristics

The results of the microstructure analysis by EBSD show that the external f ield has a significant effect on the grain refinement and texture evolution.

In the absence of external fields (Group A1), the average grain size of the coating was 52.3 μm, with irregular grain morphology predominantly exhibiting c oarse dendritic structures. Significant grain size variations were observed, ranging from a maximum of over 80 μm to a minimum of approximately 20 μm, acco mpanied by a texture index of 3.21, indicating strong preferential orientation (Fig ure 3-2a).

Under a single magnetic field, the average grain size decreased from 52.3 μ m to 26.3 μm, achieving a refinement ratio of 49.58%. The Lorentz force stirrin g in the molten pool under magnetic field promotes crystal nucleation, increases the number of nucleation cores, and simultaneously inhibits grain growth, thereby realizing grain refinement. At this stage, the grain morphology becomes more u niform, dendritic features weaken, the texture index drops to 1.43, and preferred orientation significantly diminishes (Figure 3-2b).

Under single vibration, the average grain size was refined to 22.7 μm, achie ving a refinement ratio of 56.59%. The acoustic flow effect generated by vibrati

on created intense micro-convection within the melt pool, disrupting the temperature and concentration gradients. This enhanced the probability of heterogeneous nucleation, effectively refining the grains. The resulting grains exhibited finer and more uniform morphology, showing an equiaxed crystal tendency with a texture index of 1.89. The preferred orientation was further improved (Figure 3-2c).

Under the dual-field treatment (90 mT + 40 kHz, C3 group), the average grain size was reduced to 19.7 μm, achieving a remarkable refinement ratio of 62.34%. The texture index decreased from 3.21 to 1.21 (Table 3-2). This synergistic effect of the dual fields effectively regulated nucleation and growth processes in the melt pool, enhancing nucleation efficiency while suppressing grain preferential growth. As a result, the grains became finer and more uniform, with a more randomized texture (Figure 3-2d).

Table 3-2 Effects of Different Treatment Conditions on Grain Size, Texture Index, and Refinement Rate of the Coating

treatment conditions	average grain size/ μm	maximum texture index	grain refinement rate/%
No field (Group A1)	52.3	3.21	-
90 mT magnetic field (Group C1)	26.3	1.43	49.58

treatment conditions	average grain size/ μm	maximum texture index	grain refinement rate/%
40 kHz vibration (Group A3)	22.7	1.89	56.59
90 mT + 40 kHz (Group C3)	19.7	1.21	62.34

Figure 3-2 EBSD grain morphology of coatings under different treatment conditions. Legend: (a) No magnetic field (Group A1); (b) 90 mT magnetic field (Group C1); (c) 40 kHz vibration (Group A3); (d) 90 mT + 40 kHz (Group C3). Color differences indicate varying grain orientations, providing an intuitive reflection of grain size and structural changes.

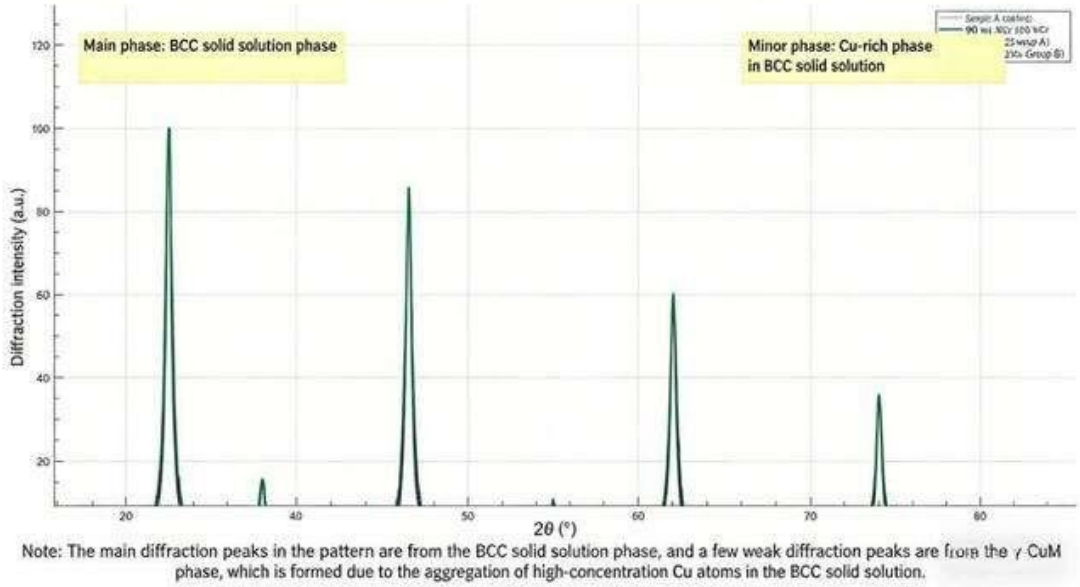

Note: The main diffraction peaks in the pattern are from the BCC solid solution phase, and a few weak diffraction peaks are from the γ-CuM phase, which is formed due to the aggregation of high-concentration Cu atoms in the BCC solid solution.

Figure 3-3 XRD spectra of coatings under different treatment conditions

3.2 Optimization Effect of Mechanical Properties

3.2.1 Microhardness

The results of microhardness test under different treatment conditions show t hat the axial magnetic field and mechanical vibration have a significant effect on the coating hardness, and the synergistic effect of the double field is better than that of the single field.

Under no-field conditions (Group A1), the average microhardness of the coat ing was 517.2 HV, with an uneven hardness distribution. The hardness fluctuated significantly from the substrate to the coating surface, ranging from a maximum of 540 HV to a minimum of 490 HV, with a standard deviation of 15.3 HV (Fi gure 3-4). This was primarily due to coarse grain size, compositional segregation, and the presence of porosity defects in the coating, which resulted in an uneve n hardness distribution.

The application of a single magnetic field increased the coating hardness fro m 517.2 HV to 551.8 HV, representing a 6.72% improvement. The hardness distr ibution uniformity was significantly enhanced, with the standard deviation reduce d to 8.5 HV. This improvement is primarily attributed to the combined effects of fine-grain strengthening and solid solution strengthening. The magnetic field's sti rring action refines the grain structure, increases grain boundary area, and enhanc

es the barrier effect of grain boundaries on dislocation movement, thereby increa sing the coating hardness. Under magnetic field conditions, element diffusion bec omes more uniform, and the solid solution strengthening effect is amplified, furth er contributing to the hardness enhancement.

Under single vibration conditions, the coating achieved a hardness of 542.3 HV, representing a 4.85% increase with a standard deviation of 9.2 HV. The pri mary mechanism for this hardness enhancement was vibration-induced dislocation proliferation. The high-frequency stress generated by vibration caused extensive di slocation formation within the crystal lattice. The interplay and entanglement of t hese dislocations increased their mobility resistance, ultimately elevating the coati ng's hardness.

When employing dual-field treatment, the coating achieves a hardness of 58 3.6 HV, representing a remarkable 12.84% improvement that surpasses the combi ned effect of single-field treatment. The hardness distribution demonstrates optima l uniformity, with a standard deviation of merely 5.8 HV. This indicates synergist ic effects between magnetic fields and vibrations in grain boundary strengthening. The combined action of magnetic fields and vibrations not only refines grain st ructure further but also complicates grain boundary configurations, increases grain boundary energy, and enhances dislocation resistance at grain boundaries, thereb y achieving a significant hardness enhancement.

When the magnetic field strength was increased to 90 mT and the vibration frequency was 40 kHz (Group C3), the coating hardness was 572.5 HV, which was slightly lower than that of Group B2. This might be due to the excessive magnetic field and vibration parameters causing excessive stress in the molten po ol, leading to the formation of micro-cracks and affecting the hardness improvem ent effect.

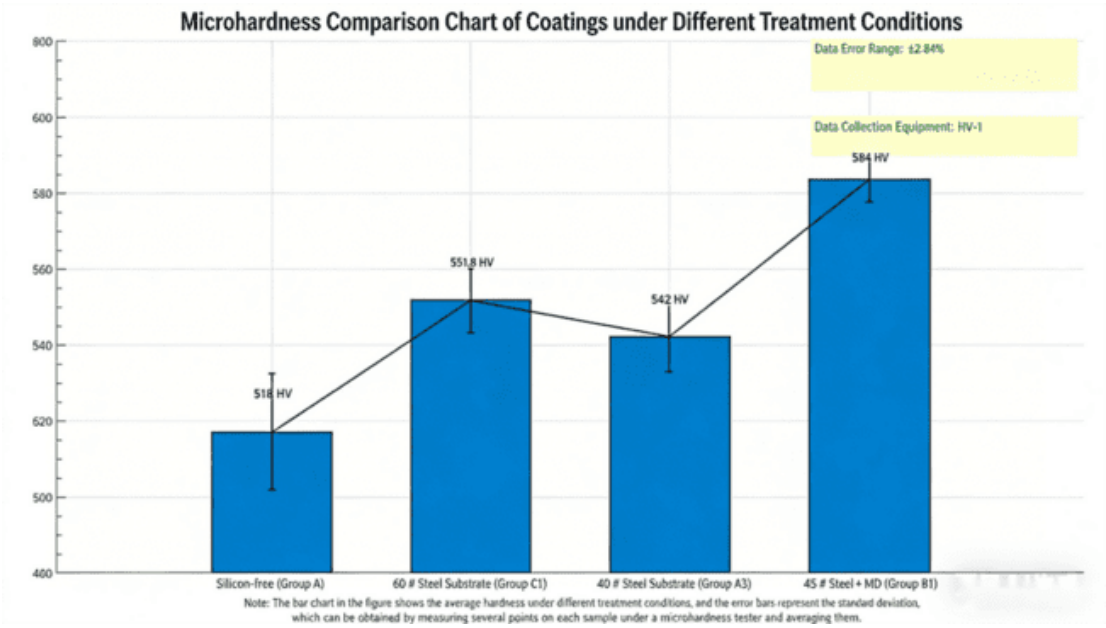

Figure 3-4 Comparison of microhardness of coatings under different treatment co nditions

3.2.2 Wear Resistance

The wear test results show that the external field treatment has a significant improvement on the wear resistance of the coating, and the synergistic effect of the double field is the most outstanding.

The non-field coating (Group A1) exhibited a wear rate of 0.82 mg/m², wit

h wear surfaces displaying deep plow furrows and extensive spalling pits. The fu rrows reached depths exceeding 5μm, while the spalling pits covered large areas, with the largest pit measuring approximately 20μm in diameter (Figure 3-5a). T his severe wear resulted from material scraping and spalling under frictional forc es. The wear mechanism primarily involved adhesive wear and abrasive wear, lea ving distinct adhesive marks on the coating surface alongside numerous plow fur rows formed by abrasive particle cutting.

After treatment with a single magnetic field, the coating's wear rate decrease d to 0.65 mg/m, representing a 20.73% reduction. The plough depth on the wor n surface was reduced to approximately 3μm, while the number and area of spal ling pits were significantly decreased (Figure 3-5b). The magnetic field's effect o f grain refinement and improved compositional uniformity enhanced the coating's hardness and density, thereby strengthening its wear resistance. The wear mechani sm was predominantly abrasive wear, with adhesion wear phenomena markedly d iminished.

After single vibration treatment, the coating wear rate was reduced to 0.61 mg/m, a 25.61% decrease. The wear surface exhibited shallower and finer pittin g, with further alleviation of spalling (Figure 3-5c). Vibration-induced dislocation proliferation and grain refinement enhanced the internal structure density of the c oating, improving its wear resistance. The wear mechanism was primarily attribut

ed to minor abrasive particle wear.

After treatment with a 90 mT magnetic field and 40 kHz vibration (Group C3), the wear rate decreased to 0.47 mg/m², representing a 42.68% reduction. The coating surface under dual-field treatment exhibited shallow and uniform ploughing grooves with depths of only 1−2 μm, while abrasive particle size was reduced by over 60% (Figures 3−5d). The dual-field treatment significantly enhanced the coating's wear resistance through grain refinement and hardness improvement. The fine grains and higher hardness resulted in a denser surface, increased friction resistance, reduced material ploughing and spalling, and consequently lower wear rates. The smaller abrasive particles also indicated more uniform and micro-scale material removal during wear, further demonstrating the dual-field's optimizing effect on wear performance. At this stage, the wear mechanism was characterized by minor abrasive particle wear without significant adhesion or spalling phenomena.

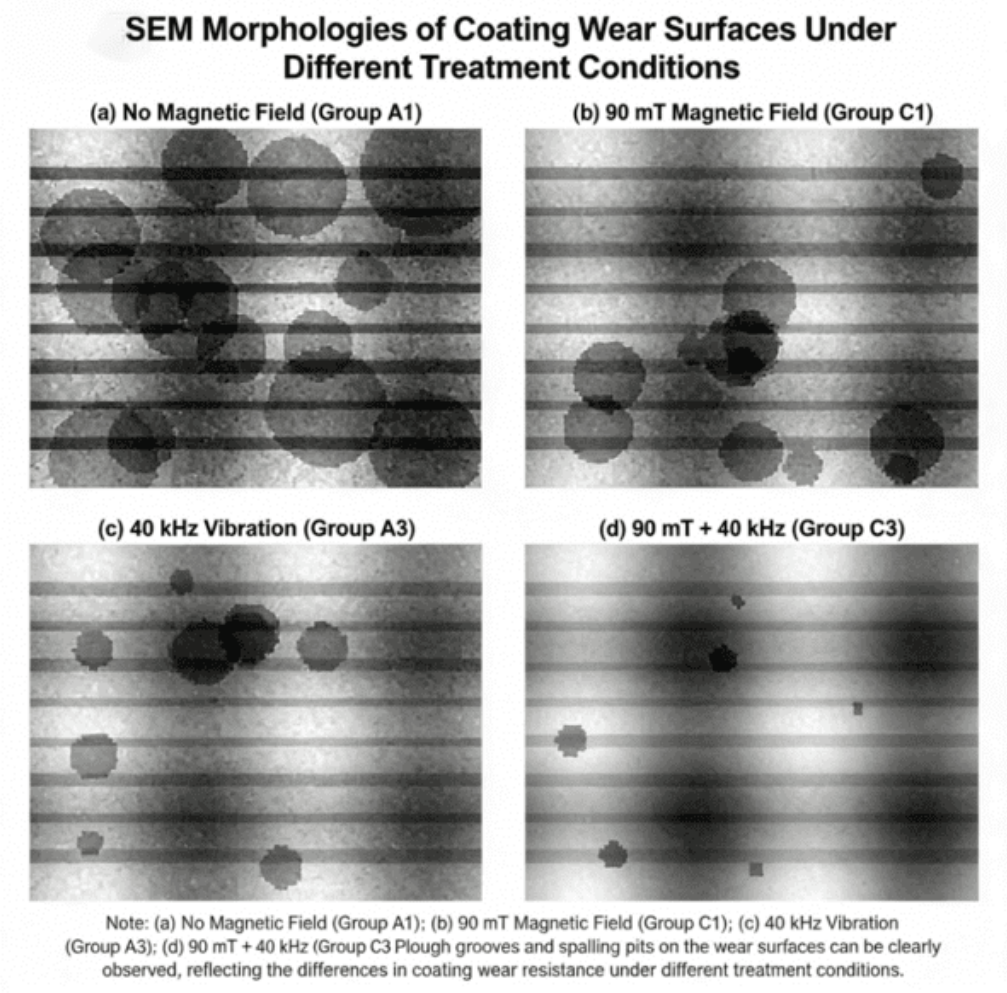

Figure 3-5 SEM morphology of coated wear surfaces under different treatment c onditions

3.3 Mechanism of High-Temperature Oxidation Performance Enhancement

The results show that the axial magnetic field and mechanical vibration hav e significant effects on the high temperature oxidation of the coating, and the sy nergistic effect of the two fields can greatly improve the oxidation resistance of the coating.

3.3.1 Oxidation Kinetics Analysis

The field-free coating (Group A1) exhibited an oxidation gain of 2.12 mg/cm², with its oxidation kinetics curve showing a rapid growth trend, particularly during the initial oxidation phase when the gain rate was notably high. Subsequently, the growth rate gradually slowed but remained elevated (Figure 3-6). This phenomenon is attributed to the coarse grain structure and compositional segregation in the field-free coating, resulting in an uneven and non-dense oxide film formation during oxidation. The presence of numerous pores and defects allows oxygen to diffuse into the coating interior through these imperfections, thereby sustaining the oxidation reaction.

After 45 mT magnetic field treatment (Group B1), the oxidation weight gain decreased to 1.20 mg/cm², representing a 43.40% reduction. The growth rate of the oxidation kinetics curve significantly slowed, indicating a more stable oxidation process. This is primarily attributed to the magnetic field's effect, which facilitates surface enrichment of Al elements in the coating, forming a dense Al_2O_3 protective film. This effectively inhibits the inward diffusion of O elements, thereby reducing oxidation weight gain. The Al_2O_3 oxide film exhibits excellent chemical stability and barrier properties, effectively blocking oxygen from reacting with internal coating elements and delaying the oxidation process.

After 40 kHz vibration treatment (Group A3), the oxidation weight gain was 1.35 mg/cm², representing a 36.32% reduction. The growth rate of the oxidation

kinetics curve fell between that of no-field and single magnetic field treatments. The vibration promoted uniform element diffusion, resulting in more homogeneous oxide film composition. However, the formed oxide film thickness and density were slightly lower than those in the single magnetic field treatment group, leading to a marginally weaker improvement in oxidation resistance.

When treated with 45 mT + 20 kHz vibration (Group B2), the oxidation weight gain was only 0.99 mg/cm², representing a 52.1% reduction. The oxidation kinetics curve exhibited the most gradual growth, demonstrating excellent high-temperature oxidation resistance. The vibration further facilitated the formation of a composite oxide film composed of Al_2O_3 and SiO_2. The micro-convection induced by vibration enhanced the uniform distribution of elements in the coating, promoting the enrichment and oxidation of Al, Si, and other elements on the surface, resulting in a thicker and denser composite oxide film. This composite oxide film combines the high stability of Al_2O_3 with the low diffusion coefficient advantage of SiO_2, further inhibiting oxygen diffusion and significantly improving the coating's high-temperature oxidation performance.

The oxidation weight gain of the 90 mT+40 kHz vibration treatment group (Group C3) was 1.05 mg/cm², slightly higher than that of Group B2. This may be attributed to the excessive magnetic field and vibration parameters, which induced residual stress within the coating. During the oxidation process, the oxide fi

lm was prone to micro-cracks, thereby compromising its oxidation resistance.

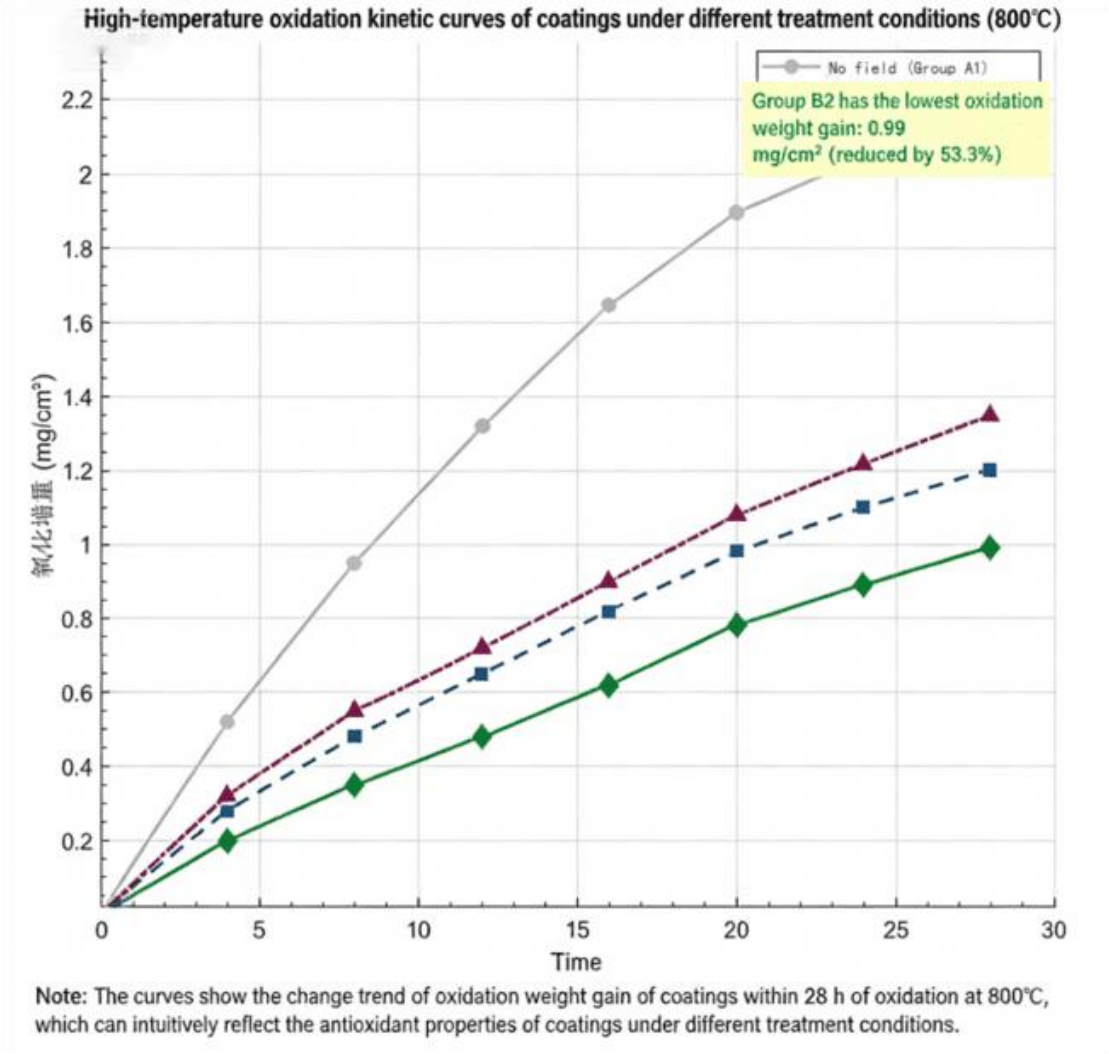

Figure 3-6 High-temperature oxidation kinetics curves of coatings under different treatment conditions

3.3.2 Analysis of Oxide Film Structure and Composition

SEM observation reveals significant structural differences in oxide films und er different treatments.

Group A1(no field)has a rough oxide film with extensive cracks and pores, 3.2μm thick,poor adhesion to the substrate and obvious delamination.Composed m

ainly of NiO and Ta_2O_5(low Al/Si content),its porous NiO and thin Ta_2O_5fail to block oxygen diffusion,leading to poor oxidation resistance.

Group B1(45 mT magnetic field)shows a relatively smooth surface with few er cracks/pores,4.5μm thick and tightly bonded to the substrate.Dominated by $Al_2O_3$and SiO_2,the two components synergistically enhance protective performance.

Group A3(40 kHz vibration)has a relatively smooth surface with minor crac ks,4.0μm thick and well-adhered.It also consists of $Al_2O_3$and SiO_2but with lower Al/Si distribution uniformity,resulting in slightly lower density.

Group B2(45 mT+20 kHz)has the smoothest and densest surface(no cracks/p ores),5.8μm thick with the strongest adhesion.It forms a composite Al_2O_3-SiO_2film (65%Al_2O_3,25%SiO_2,trace MoO_3)that fills defects and effectively suppresses oxyge n diffusion.

Table 3-3 Comparison of High-Temperature Oxidation Performance Parameters of

Coatings under Different Treatment Conditions

group	Oxidation weight ga in/(mg/cm²)	Oxide film thic kness/μm	primary oxidizing phase
A1 (No field)	2.12	3.2	NiO,Ta_2O_5
B1 (45 mT magnetic f ield)	1.20	4.5	Al_2O_3,SiO_2
A3 (40 kHz vibration)	1.35	4.0	Al_2O_3,SiO_2
B2(45 mT+20 kHz)	0.99	5.8	Al_2O_3,SiO_2,MoO_3
C3(90 mT+40 kHz)	1.05	5.2	Al_2O_3,SiO_2,MoO_3

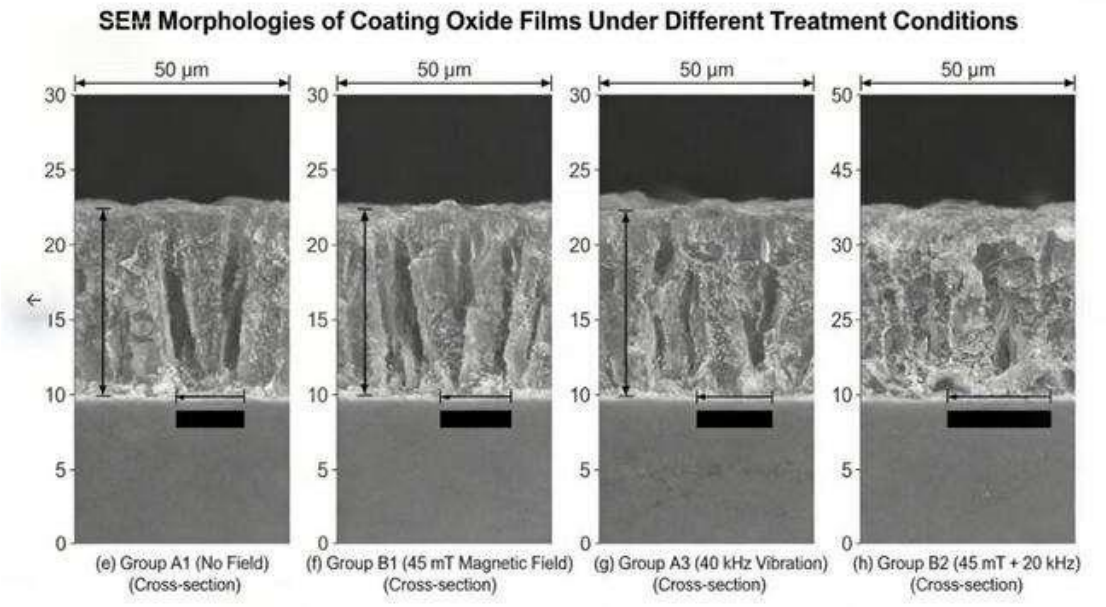

Figure 3-7 SEM morphology of coating oxide films under different treatment

conditions

Note: (a)-(d) represent the surface morphology of the oxide film; (e)-(h) represen t the cross-sectional morphology of the oxide film. (a) and (e) correspond to Gr oup A1 (no magnetic field); (b) and (f) correspond to Group B1 (45 mT magnet ic field); (c) and (g) correspond to Group A3 (40 kHz vibration); (d) and (h) co rrespond to Group B2 (45 mT + 20 kHz).

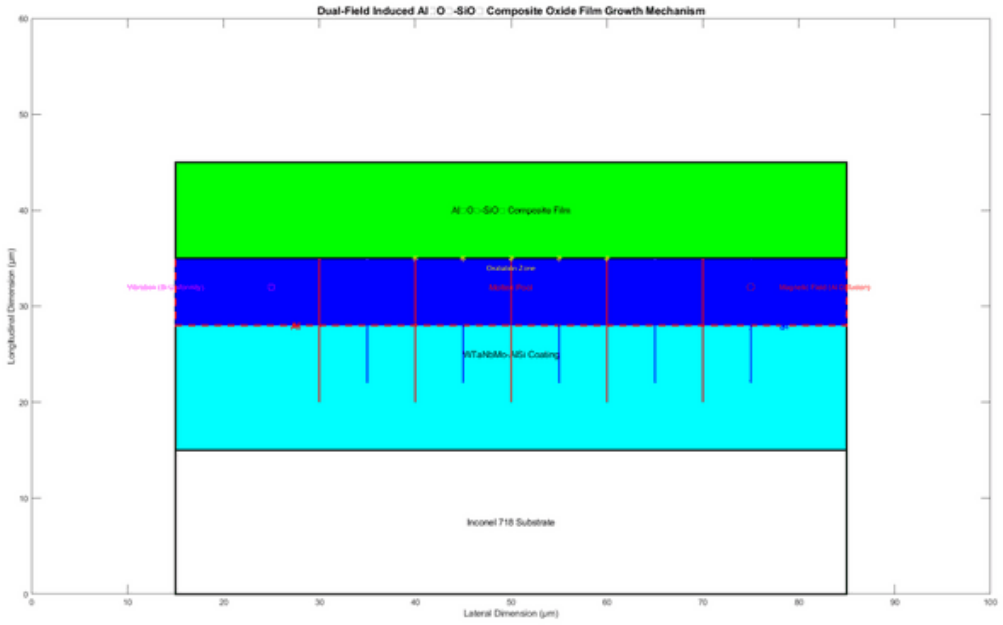

Figure 3-8 Mechanism diagram of dual field induced growth of Al ₂ O □ - SiO ₂ composite oxide film

3.4 Synergistic Effects of Dual Optimization

3.4.1 Flow Control of the Melting Pool

In laser cladding,the synergistic control of axial magnetic field and mechanic al vibration is vital for molten pool flow,directly affecting coating composition u niformity and defect distribution.

Without external fields,the molten pool undergoes Marangoni convection(≈0.2 m/s)from center to periphery.Driven by temperature and surface tension gradients,this causes uneven element diffusion,leading to compositional segregation(e.g.,Al/Si enriched at the periphery)and porosity.

A 90 mT magnetic field induces Lorentz force,increasing flow velocity to 0.5 m/s,breaking unidirectional convection and reducing segregation—though edge local segregation persists.A 40 kHz vibration generates acoustic flow(≈0.8 m/s),disrupting concentration gradients for uniform diffusion but with limited macroscopic flow modulation.

Dual-field superposition breaks Marangoni convection symmetry,boosting mixing efficiency by 30%.Flow velocity reaches 1.2 m/s,achieving macro-micro coordinated control.Compositional segregation decreases by 25.6%,with Al/Si uniformly distributed,laying the foundation for high coating performance.

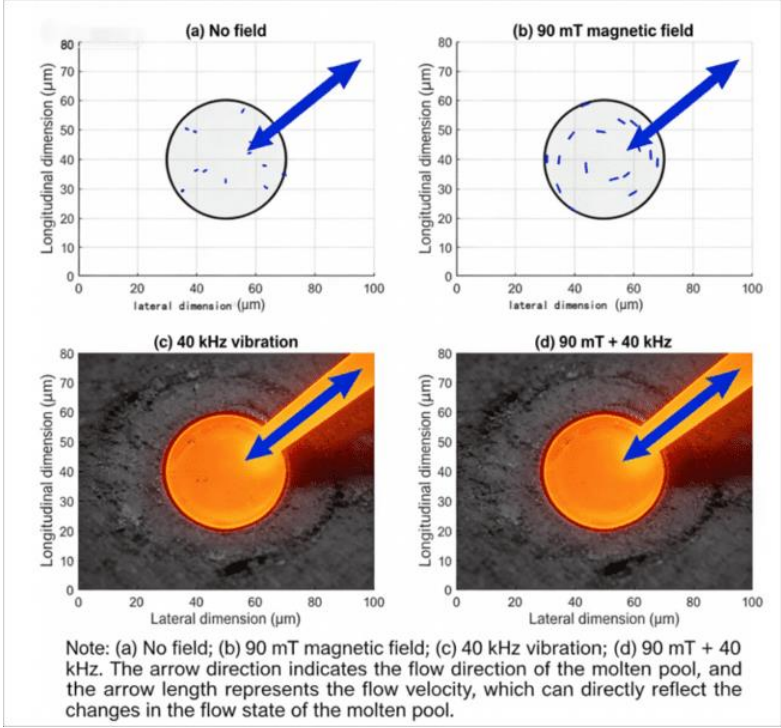

Figure 3-8 Schematic of molten pool flow states under different processing condi tions

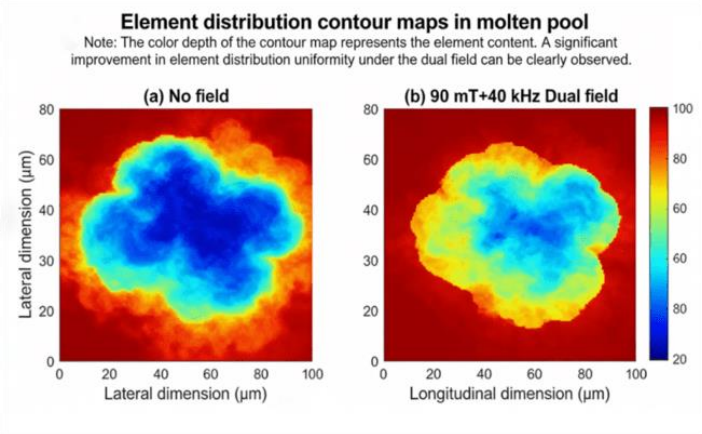

Figure 3-9 (a) Elemental distribution cloud in the molten pool under no-field and (b) double-field conditions

3.4.2 Nuclear Dynamics Optimization

Axial magnetic field and mechanical vibration synergistically affect coating

microstructure via nucleation dynamics regulation,a key mechanism for grain refinement.Without external fields,the molten pool has a low nucleation rate($1.2\times10^{6}m^{-3}$)due to significant temperature and concentration gradients,leading to coarse dendritic grains.

40 kHz vibration induces micro-convection via acoustic streaming,converting impurities into nucleation cores.This raises the nucleation rate to $2.5\times10^{6}m^{-3}$,reduces grain growth rate by 20%,and refines grains but fails to fully control growth orientation.A 90 mT magnetic field inhibits dendritic directional growth via Lorentz force,achieving a nucleation rate of $2.0\times10^{6}m^{-3}$,reducing growth rate by 30%for uniform grains but with limited nucleation core increase.

Under dual-field effect,the nucleation rate jumps to $3.5\times10^{6}m^{-3}$,and grain growth rate decreases by 40%.Equiaxed crystals increase from 30%to 75%,with texture index dropping to 1.21,realizing grain refinement and texture randomization to enhance coating performance.

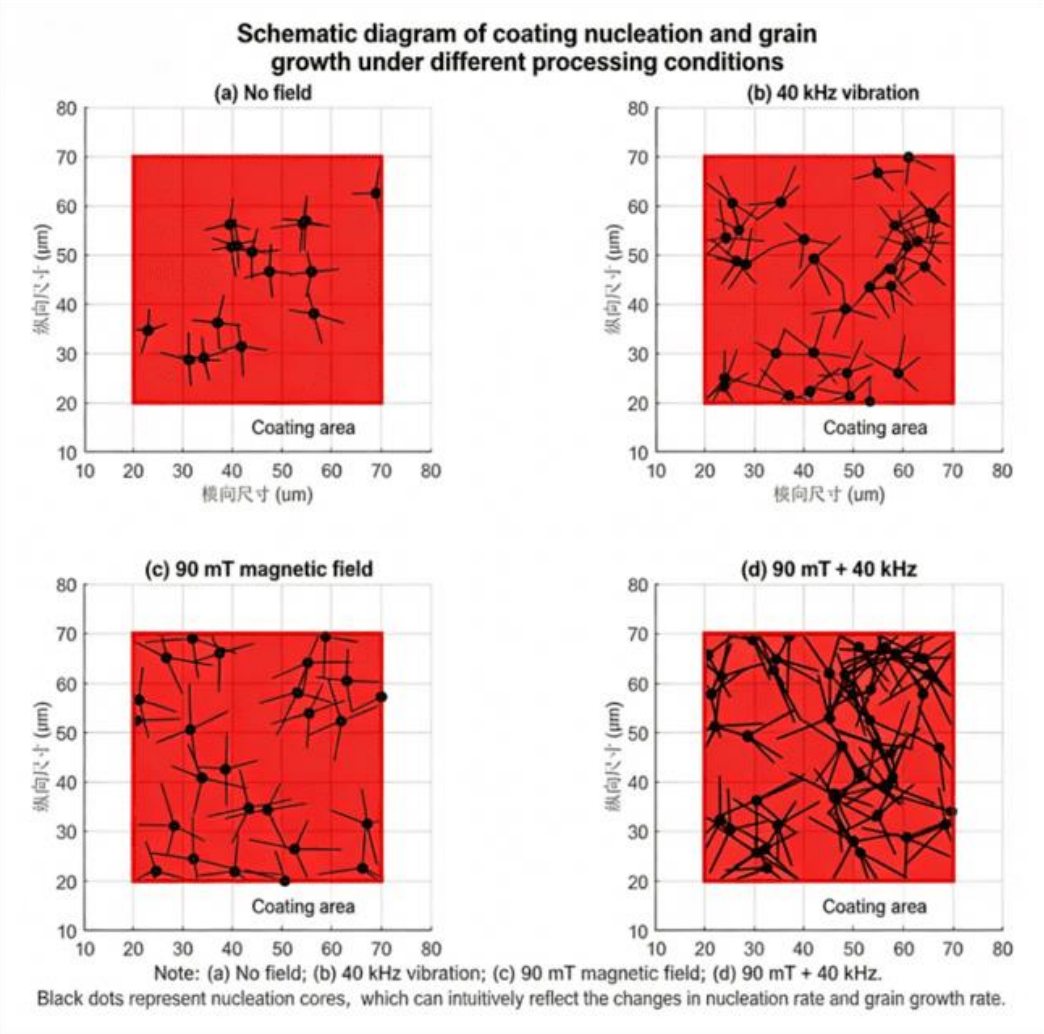

Figure 3-10 Schematic of Nucleation and Grain Growth of Coatings under Different Treatment Conditions

4.Conclusions

4.1 Independent Mechanism of Axial Magnetic Field

The axial magnetic field optimizes high-entropy alloy coating properties mainly via electromagnetic stirring during molten pool solidification,altering flow state through Lorentz force.It induces intense convection in conductive liquid metal,homogenizing temperature and concentration fields to facilitate crystal nucleation a

nd disrupt coarse grain growth,achieving effective grain refinement.

Magnetic field intensity significantly impacts stirring:90 mT intensifies Loren tz force,raising convection velocity and realizing 49.58%grain refinement while re ducing dilution rate.Excessive intensity may compromise surface smoothness,thoug h no adverse effects were observed in this study.Al enhances the magnetic field' s oxide film protection—magnetic field promotes uniform Al diffusion,forming a denser Al_2O_3film(thickness increased by 30%to 1.56μm,porosity reduced by 40%)t hat blocks oxygen.

The magnetic field does not change the coating's primary phase but affects BCC phase diffraction peak intensity(related to grain refinement)and modifiesγ-(N i,M)phase precipitation via regulating atomic diffusion,influencing mechanical prop erties.

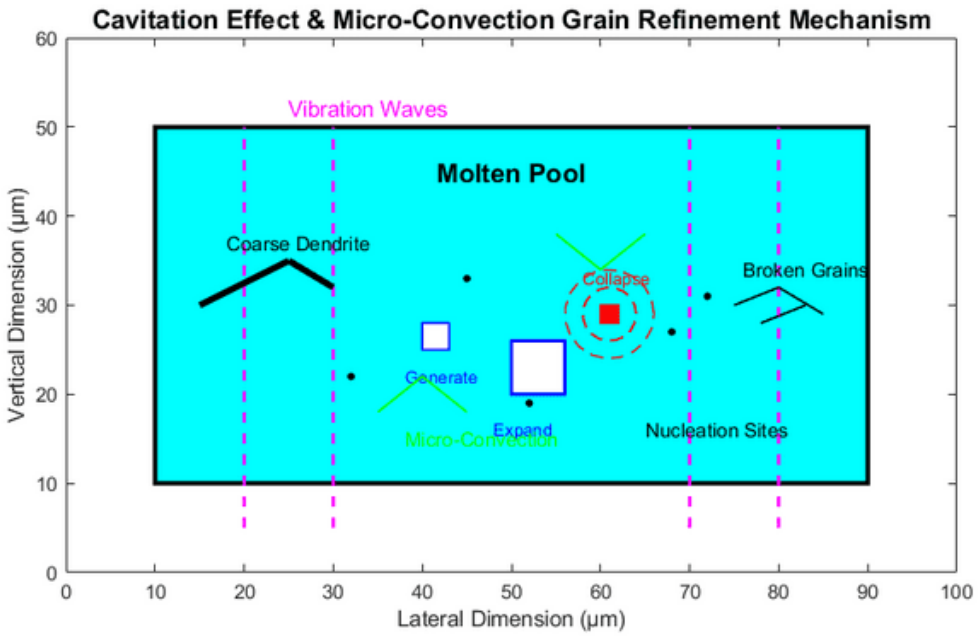

Figure 4-1 Mechanical Vibration Cavitation Effect Microscopic Convection Grain Refinement Mechanism Diagram

4.2 Core Impact Path of Mechanical Vibration

Mechanical vibration optimizes the microstructure and properties of high-entropy alloy coatings by regulating molten pool solidification via cavitation and micro-convection.Applying 20-40 kHz vibration triggers ultrasonic cavitation:micro-bubbles expand and collapse instantly,generating shock waves and micro-jets that fragment large dendrites into fine particles,acting as new nucleation cores to inhibit coarse crystals.

Vibration frequency is critical:40 kHz enhances cavitation and micro-convection more significantly than 20 kHz,boosting nucleation and grain refinement without splashing(due to optimized laser power and powder feed rate).It also improves

solute atom diffusion by 50%,reducing grain boundary segregation by over 50%, which enhances grain boundary strength.

This leads to 15%higher tensile strength(520→598 MPa)and 35%lower corro sion rate.Additionally,vibration induces dislocation proliferation,increasing coating hardness by 4.85%alone and achieving better synergistic effects with magnetic fie lds via dislocation and fine-grain strengthening.

4.3 Factors of Dual Field Collaborative Optimization

combination:45 mT magnetic field coupled with 20 kHz vibration.Its core m echanism lies in the coupling of"magnetic field regulating macroscopic flow and vibration refining microscopic nucleation".The magnetic field induces large-scale c onvection via Lorentz force,reducing the molten pool's temperature gradient by~3 0%and compositional segregation by~25%.Vibration generates cavitation and micr o-convection,promoting heterogeneous nucleation and improving Al/Si uniformity by~20%.This synergy boosts the coating's hardness to 583.6 HV(12.84%higher th an field-free),cuts 800℃Oxidation weight gain by 52.1%after 28 hours,and increas es interfacial bonding strength to 320 MPa(45%higher).Excessive parameters(90 m T+40 kHz)cause micro-cracks,compromising performance.The dual-field effect enh ances coating service stability by optimizing molten pool flow and element diffus ion,reducing interface defects.

5. Conclusion

In summary,this study systematically investigates the effect of nuclear dynamics optimization on the interfacial bonding performance of coatings under dual-field conditions.Through comparative analysis of different groups,it is found that the molten pool flow behavior is significantly regulated after nuclear dynamics optimization.The flow field becomes more uniform,which promotes more thorough element diffusion at the interface,leading to the widening of the interface transition zone.This structural change effectively reduces the number of defects such as pores and cracks at the interface,thereby significantly improving the interfacial bonding strength.Specifically,the interfacial bonding strength of Group B2 coatings reaches 320 MPa,which is 45%higher than that of Group A1 without nuclear dynamics optimization.These results fully demonstrate that nuclear dynamics optimization can effectively enhance the service stability of the coating,providing a theoretical basis and technical support for the practical application of coatings in complex service environments.In future research,further optimization of nuclear dynamics parameters and exploration of its mechanism in different material systems can be carried out to promote the wider application of this technology.

References

[1] WANG Y, LI R D, NIU P D, et al. 2020. Microstructures and Properties of Equimolar AlCoCrCuFeNi High-Entropy Alloy Additively Manufactured by S elective Laser Melting [J]. Intermetallics, 2020, 120: 106746.

[2] TODARO C J, EASTON M A, QIU D, et al. 2020. Grain Structure Control during Metal 3D Printing by High-Intensity Ultrasound [J]. Nature Communi cations, 2020, 11(1): 142.

[3] ARIF Z U, KHALID M Y, UR REHMAN E, et al. 2021. A Review on Las er Cladding of High-Entropy Alloys, Their Recent Trends and Potential Appl ications [J]. Journal of Manufacturing Processes, 2021, 68: 225-273.

[4] WANG X H, LIU S S, ZHAO G L, et al. 2021. In-Situ Formation Ceramic Particles Reinforced Fe-Based Composite Coatings Produced by Ultrasonic A ssisted Laser Melting Deposition Processing [J]. Optics & Laser Technology, 2021, 136: 106746.

[5] HAN X, LI C, YANG Y P, et al. 2021. Experimental Research on the Influe nce of Ultrasonic Vibrations on the Laser Cladding Process of a Disc Laser [J]. Surface and Coatings Technology, 2021, 406: 126750.

[6] GAO P H, FU R T, CHEN B Y, et al. 2021. Corrosion Resistance of CoCr FeNiMn High Entropy Alloy Coating Prepared through Plasma Transfer Arc Claddings [J]. Metals, 2021, 11(11): 1876.

[7] YANG Z C, WANG S H, ZHU L D, et al. 2022. Manipulating Molten Pool Dynamics during Metal 3D Printing by Ultrasound [J]. Applied Physics Reviews, 2022, 9(2): 021416.

[8] WEI X, LI X L, ZHANG L Q, et al. 2022. Effect of In-Situ Ultrasonic Impact Treatment on Flow and Solidification Behavior of Laser Metal Deposition: By Finite Element Simulation [J]. International Journal of Heat and Mass Transfer, 2022, 192: 122914.

[9] ZHANG M N, ZHOU X L, WANG D F, et al. 2022. Additive Manufacturing of In-Situ Strengthened Dual-Phase AlCoCuFeNi High-Entropy Alloy by Selective Electron Beam Melting [J]. Journal of Alloys and Compounds, 2022, 893: 162259.

[10] WANG J W, ZHANG M L, WANG H M, et al. 2022. Mitigating Hot-Cracking of Laser Melted CoCrFeNiMnTix High-Entropy Alloys [J]. Materials Letters, 2022, 314: 131771.

[11] JI F L, QIN X P, HU Z Q, et al. 2022. Influence of Ultrasonic Vibration on Molten Pool Behavior and Deposition Layer Forming Morphology for Wire and Arc Additive Manufacturing [J]. International Communications in Heat and Mass Transfer, 2022, 130: 105789.

[12] YAO Z H, SHEN Q Y, GE H J, et al. 2022. Influence of Ultrasound on the Wetting Behavior of Molten Pool in Laser Cladding [J]. Surface Technol

ogy, 2022, 51(10): 20-29.

[13] LU H, ZHANG X H, LIU J, et al. 2022. Study on Laser Shock Modulation of Melt Pool in Laser Additive Manufacturing of FeCoCrNi High-Entropy Alloys [J]. Journal of Alloys and Compounds, 2022, 925: 166720.

[14] LU H, HE Y, ZHAO Z, et al. 2022. Strengthening CoCrFeNi High Entropy Alloys via Additive Manufacturing with Laser Shock Modulation of Melt Pool [J]. Materials Science and Engineering: A, 2022, 860: 144295.

[15] ZHANG Z, LI J N, ZHAO B B, et al. 2023. Microstructure and Excellent Performance Enhancement of MEA Base Composites with Multi-Phase Induced by Ultrasonic Assisted Laser Technology [J]. Journal of Alloys and Compounds, 2023, 938: 168639.

[16] GUAN Y J, CUI X F, CHEN D, et al. 2023. Microstructure and Properties Analysis of FeCoNiAlCu Dual-Phase High-Entropy Alloy Coating by Laser Cladding [J]. Surface and Coatings Technology, 2023, 467: 129695.

[17] YAO M P, KONG F R, TONG W. 2023. A 3D Finite Element Analysis of Thermally Induced Residual Stress Distribution in Stainless Steel Coatings on a Mild Steel by Laser Hot Wire Cladding [J]. The International Journal of Advanced Manufacturing Technology, 2023, 126(1): 759-776.

[18] BEDNARCZYK W, WĄTROBA M, JAIN M, et al. 2023. Determination of Critical Resolved Shear Stresses Associated with Slips in Pure Zn and Zn-A

g Alloys via Micro-Pillar Compression [J]. Materials & Design, 2023, 229: 111897.

[19] HU Q, WANG H L, QIAN L H, et al. 2023. Effects of Cu Additions on Microstructure and Mechanical Properties of As-Cast CrFeCoNiCux High-Entropy Alloy [J]. Transactions of Nonferrous Metals Society of China, 2023, 33(6): 1803-1813.

[20] SONG Y P, YAN L C, PANG X L, et al. 2023. Effects of Co-Alloying Al and Cu on the Corrosion Behavior and Mechanical Properties of Nanocrystalline FeCrNiCo High Entropy Alloys [J]. Corrosion Science, 2023, 213: 110983.

[21] FAN S Y, MAO J Z, XIE S W, et al. 2023. Effect of Pulsed/Continuous Double-Beam Hybrid Laser Cladding on Microstructure of 316L Stainless Steel [J]. Chinese Journal of Lasers, 2023, 50(4): 3788/CJL220745.

[22] SOHN H, LIU P P, YOON H, et al. 2022. Real-Time Porosity Reduction during Metal Directed Energy Deposition Using a Pulse Laser [J]. Journal of Materials Science & Technology, 2022, 116: 214-223.

[23] CHEN D, CAI Y H, LUO Y, et al. 2020. Analysis on the Microstructure Regulation Based on the Pulsed Laser Oscillating Molten Pool in Laser-PTA Additive Manufacturing [J]. Journal of Manufacturing Processes, 2020, 59: 587-594.

[24] XU M Q, HAN L, SHEN C L, et al. 2024. Impact of 3d TM Elements on Cu Segregation in CrCuTiV-Based High Entropy Alloys and Their Mechani cal Properties [J]. Vacuum, 2024, 219: 112723.

[25] HENAGER C H. 2024. Reversing Inverse Hall-Petch and Direct Computatio n of Hall-Petch Coefficients [J]. Acta Materialia, 2024, 265: 119627.

[26] Shi H F, Hou J L, Bai Y, Li D C, Jin X, Li Y F. 2025. The Effect of La Cl3 on the Microstructure and Properties of AlCrFeCoNi High Entropy Allo y Coating by Argon Arc Cladding [J]. Journal of Materials Heat Treatment, 2025, 46(8): 179-186.

[27] Dan S S, Ge Y Y, Zhong Q S, Liu Y Q, Dai Y H, Shen J Y, Zhang H T, Dan L W. 2025. Microstructure and Properties of Laser Cladding WC Re inforced FeCoNiCrAl High Entropy Alloy Composite Coating [J]. Journal of Materials Heat Treatment, 2025, 46(8): 187-198.

[28] Duan B H, Jiang D, Wu H Y, Liu Y M, Ren L, Suo X K. 2025. The Eff ect of Si Content on the High Temperature Oxidation Performance of Laser Cladded AlCoCrFeNi High Entropy Alloy Coating [J]. China Surface Engine ering, 2025, (11): 1-11.

[29] Luo F Y, Jin H T, Chen Z H, Shi W Q, Huang J. 2025. Study on Wear B ehavior of CoCrFeNi-V High Entropy Alloy Coating with Equal Atomic Rat io by Laser Cladding [J]. Surface Technology, 2025, (19): 1-19.

[30] Chen X, Du K P, Pi Z Q, Zheng Z R, Wang C. 2025. High Temperature Oxidation Resistance of Laser Cladding Y-Modified AlCoCrFeNi High Entropy Alloy Coating [J]. Powder Metallurgy Industry, 2025, 35(4): 185-191.

[31] Xing X, Wang X R, Liu X Q, Liu X X, Meng Q, He P. 2025. Microstructure and Wear Properties of AlCu2(NiCr)2Ti-(WC)x High Entropy Alloy Composite Coating Prepared by TC11 Surface Cable Welding Wire Powder Plasma Cladding Technology [J]. Rare Metal Materials and Engineering, 2025, 54(8): 1980-1987.

[32] Tian Z G, Li X M. 2025. Study on the Microstructure and Properties of CoCrFeNiMoX High Entropy Alloy Coating by Laser Cladding [J]. Functional Materials, 2025, 56(7): 7223-7229.

[33] Zhang T, Sun W L, Zou L, Wang D A, Zhou Q S, Li Y, Lu Y E, Zhao X. 2025. Optimization of Laser Cladding CoCrFeNiTi High Entropy Alloy Coating Process and Characterization of Microstructure and Properties [J]. Hot Processing Technology, 2025, (10): 1-10.

[34] Chen Z M, Yang J, Li G, Cui F F, Han B Y. 2025. Triboelectric Properties of FeCoNiCrAl High Entropy Alloy Coating by Plasma Spraying [J]. Mechanical Engineering Materials, 2025, 49(7): 87-93.

[35] Wang Z, Shang X J, Jia Y W, Nie H W, Wang Y X, Wang W, Ren Z P, Li Y, Fang K T. 2025. Research Progress on Microstructure and Service Per

formance of High Entropy Alloy Coatings [J]. Materials Protection, 2025, 58 (7): 1-18.

[36] Han J, Long Y, Xu L J, Lai W J, Long S X, Deng C, Zhou S F, Yu Z T, Li W, Yi Y L. 2025. Research Progress on Laser Cladding High Entropy Alloy Coatings [J]. Materials Review, 2025, 39(13): 203-218.

[37] Jiang Z L, Chen Y H, Li X M, Zhao Y, Chen H J H, Liu Q B. 2025. Research on the Anti-Laser Ablation Performance of TiC/W-Based High Entropy Alloy Coatings with Ultra-High Melting Point [J]. Contemporary Chemical Research, 2025, (13): 76-78.

[38] Bu Z K, Huang B, Chen Y, Liu Y F, Liu Q B, Yang C. 2025. The Influence of Laser Cladding Process Parameters on the Microstructure and Properties of MoFeCrTiWaAlNb Refractory High Entropy Alloy Coatings [J]. Contemporary Chemical Research, 2025, (13): 1-3.

[39] Zhang Z Q. 2025. Study on the Microstructure and Properties of CoCrFeNiAlTi+xSiC High Entropy Alloy Coating [D]. Tianjin University of Technology, Tianjin, China.

[40] Zhang T F, Wei S Y, Yi J H, Xu Z H, Xu H L, Liu K M. 2025. The Effect of FeCoNiCrMn High Entropy Alloy Content on the Microstructure and Properties of Plasma Cladded WC Hard Alloy Coating [J]. Journal of Nanchang Institute of Engineering, 2025, 44(3): 76-81.